Published on 09 September 2021. Downloaded by National Synchrotron Radiation Research on 11/8/2021 6:47:33 AM.

Soft Matter

ROYAL SOCIETY OF CHEMISTRY

PAPER

View Article Online
View Journal | View Issue

Check for updates

Cite this: *Soft Matter*, 2021, **17**, 9189

Phase behavior in thin films of weakly segregated block copolymer/homopolymer blends†

Jia-Wen Hong, Jung-Hong Chang, Iris Ching-Ya Chang and Ya-Sen Sun *

Received 8th July 2021,
Accepted 7th September 2021

DOI: 10.1039/d1sm01005k

rsc.li/soft-matter-journal

We have demonstrated the phase behavior of substrate-supported films of a symmetric weakly segregated polystyrene-*block*-poly (methyl methacrylate), P(S-*b*-MMA), block copolymer and its blends with homopolymer polystyrene (PS) at different compositions. Upon increasing the content of added PS in the blends, lamellae (L), perforated layers (PL), double gyroid (DG) and cylinders (C) are obtained in sequence for films. Among these nanodomains, PL and DG only exist in a narrow ϕ_{PS} region (ϕ_{PS} denotes the volume fraction of PS). At ϕ_{PS} = 64%, tuning film thickness and annealing temperature can produce parallel PL or DG with $\{121\}_{DG}$ lattice planes being parallel to the substrate surface. The effects of annealing temperature and film thickness on the formation of PL and DG are examined. In thin films with $n \approx 3$ (n denotes the ratio of initial film thickness to inter-domain spacing), the PL phase solely exists regardless of temperature. However, for thick films with $n \approx 6$ and 10, thermal annealing at the most accessible temperature produces films containing both PL and DG of various fractions, but a low temperature tends to favor a greater fraction of PL. The PL phase becomes the only discernible phase if thick films are shortly annealed at 230 °C.

1. Introduction

It has been well established that the equilibrium phase behavior in bulk for block copolymers (BCPs) can be tailored by the segregation strength (χN) and volume fractions (f) of constituent blocks, where χ denotes the Flory–Huggins interaction and N denotes the degree of polymerization. Below an order–disorder transition temperature, a series of classic nanodomains such as lamellae (L), cylinders (C), double gyroid (DG) and spheres (S) can be obtained through the self-assembly of BCPs.[1] However, as BCPs are prepared as thin films on a supported solid substrate, the synergistic effects of surface fields and spatial confinement can produce a different phase behavior, which deviates from bulk morphologies.[2–12] For thin films of asymmetric and symmetric BCPs, tuning surface fields and/or changing film thickness can form several non-bulk structures. Even different non-bulk structures can coexist laterally in the same plane or vertically at different depths.[6–12] Also, domain orientation, and shape or size undulation are influenced by both spatial confinement and surface fields.[13–21]

Furthermore, thickness-dependent order–disorder and order–order phase transitions and lattice packing of thin films can differ from those of the BCP bulk. The first example is the breaking of lattice symmetry from body-centered cubic (BCC) to face-centered orthorhombic (FCO) and to hexagonal close packing (HCP), which has been observed in sphere-forming polystyrene-*block*-poly (2-vinylpyridine), P(S-*b*-2VP), BCP thin films.[22–24] At a highly asymmetric volume fraction, P(S-*b*-2VP) BCPs tend to form ordered spheres with BCC lattices in bulk. In thick films, the BCC (110) planes of ordered spheres are preferentially oriented parallel to the substrate surface. As film thickness decreases, lattice symmetry breaks from a BCC-based lattice to an FCO-based lattice. As the layer thickness is less than tri-layers, 2D hexagonal arrays become a favorable packing.[22–24] The second example is the stabilization of hexagonally perforated layers in thin films for the double gyroid of a weakly segregated BCP bulk.[25,26] Previous studies have demonstrated that the double gyroid is an equilibrium phase and hexagonally perforated layers are a long-live metastable phase.[27–33] The main reason is that perforated layers have higher packing frustration than the double gyroid.[34] However, spatial confinement can stabilize hexagonally perforated layers and close-packed spheres. Even order–disorder transition

Department of Chemical and Materials Engineering, National Central University, Taoyuan 32001, Taiwan. E-mail: yssun@cc.ncu.edu.tw

† Electronic supplementary information (ESI) available: Fig. S1 optical images of thin blend films. Fig. S2 AFM topography of a terraced film. Fig. S3 AFM topographies of thin blend films before and after oxygen plasma etching. Fig. S4 height profiles of a lamellar-forming film with and without oxygen plasma etching of varied duration. Fig. S5 PSD profiles of a lamellar-forming film with and without oxygen plasma etching of varied duration. Fig. S6 Magnified AFM topographic and phase images of coexistence of two phases as well as the presence of the DG phase. Fig. S7 AFM topographies of films annealed at 230 °C for blends of high-molecular-weight P(S-*b*-MMA) BCPs with PS. Fig. S8 AFM topographies of films annealed at 270 °C for blends of high-molecular-weight P(S-*b*-MMA) BCPs with PS (need a revision when all the figures are settled down). See DOI: 10.1039/d1sm01005k

Published on 09 September 2021. Downloaded by National Synchrotron Radiation Research on 11/8/2021 6:47:33 AM.

temperatures[35–38] and the kinetics of spatial ordering[39] were found to differ at different thicknesses.

In addition to spatial confinement, adding a homopolymer to a copolymer melt not only causes morphological changes but also affects the relative stability of various morphologies.[40–42] The morphological changes are due to the variations in the volume fraction of the constituent block. New phases are stabilized by a way that homopolymer chains fill the space originally occupied by highly stretched copolymer chains.[43,44] Such a way can alleviate the packing frustration of stretched copolymer chains. For example, Huang *et al.* found BCC-to-FCC order–order transitions in sphere-forming block copolymer/homopolymer blends.[45] Chu *et al.* found the stabilization of order bi-continuous double-diamond structures.[46] Wang *et al.* found that the addition of low-molecular-weight oligomers can lead to order–order transition from a helical phase to the double-gyroid phase.[47] Mishra *et al.* found that the addition of a homopolymer can stabilize FCO phases in thin films.[23] Adding small molecules into a BCP through supramolecular self-assembly is another strategy to obtain a variety of nanodomains.[48,49] These studies mentioned above demonstrated that adding a homopolymer or small molecule into BCPs can increase morphological diversity, amplify size tunability and enhance phase stability.

The introduction of spatial confinement and surface fields even increases the level of complexity of self-assembly in thin films of BCP/homopolymer mixtures.[50–57] Furthermore, homopolymer addition also influences the kinetics and dynamics of spatial ordering of nanodomains in thin films.[58,59] All the studies focused on phase behavior in thin films of BCPs that form classic structures such as lamellae, cylinders and spheres. However, to the best of our knowledge, only less attention has been paid to perforated layers and double gyroid in thin films of binary blends of a weakly segregated BCP with a homopolymer of low molecular weight.

Because of the easy degradation of PMMA blocks with UV-light exposure, P(S-*b*-MMA) films can offer a versatile platform to make porous membranes for drug delivery[60] and foreign-impurity separation.[61,62] Perpendicular-oriented cylinders are frequently used for membrane applications. However, if the perpendicular orientation is not perfect over the whole thickness of a film for cylinders, membrane separation becomes ineffective. To solve this problem, interconnected bi-continuous porous channels are further surveyed.[61,62] The double gyroid phase has an interconnected network and can serve as building blocks to fabricate porous membranes with an interconnected framework.[62] Nevertheless, to our knowledge, obtaining ordered double gyroid is rarely reported for the thin film system of P(S-*b*-MMA) BCPs. To obtain long-range order for double gyroid generally needs solvent annealing.[63] However, devices of solvent annealing are only limited to lab scale and have not been realized yet in real industrial manufacturing.

This study aims to systematically study the phase behavior of thin films of a weakly segregated P(S-*b*-MMA) and its miscible blends with homopolymer polystyrene (PS) of low molecular weight at various weight fractions. The homopolymer PS has a lower molecular weight than the PS and PMMA blocks. Upon finely tuning the weight fraction, film thickness and temperature, we can obtain several nanostructures including lamellae, perforated layers, double gyroid and cylinders. All the nanodomains were obtained simply by brief thermal annealing. In the first section, we first study the effects of PS contents on the phase behavior in thin films and clarify the existing ϕ_{PS} ranges for the obtained nanodomains. In the second section, we study the effects of thickness and temperature on the formation of perforated layers and double gyroid at ϕ_{PS} = 64% under spatial confinement in films.

2. Experimental section

2.1. Materials and sample preparation

The nearly-symmetric P(S-*b*-MMA) BCP (M_n^{PS} = 21 kg mole^{-1} and M_n^{PMMA} = 21 kg mol^{-1}, f_{PS} = 52%, and $Đ$ = 1.07) and a low-molecular-weight PS homopolymer (M_n = 6 kg mol^{-1}, $Đ$ = 1.33) were purchased from Polymer Source Inc., and used as received. P(S-*b*-MMA) was first dissolved in toluene to prepare P(S-*b*-MMA) solutions. Various amounts of PS were added to blend with the P(S-*b*-MMA) to give P(S-*b*-MMA)/PS mixtures in toluene. Eight weight-fraction ratios were prepared for P(S-*b*-MMA)/PS binary blends: 95/5, 85/15, 80/20, 75/25, 70/30, 65/35, 60/40 and 50/50. The total volume fractions (ϕ_{PS}) of PS were estimated to be 55, 60, 62, 64, 67, 69, 72, and 77 vol% from the experimentally determined weight fractions and homopolymer densities: ρ_{PS} = 1.06 and ρ_{PMMA} = 1.15 g cm^{-3}. Two polymer weight fractions (3 and 5 wt%) in toluene were prepared. Films of neat P(S-*b*-MMA) and P(S-*b*-MMA)/PS mixtures were prepared by spin coating from the solutions onto substrates. The thickness of the films was controlled by using different concentrations and spin rates. Three initial thicknesses (h_i) obtained were approximately 97 nm (3 wt%, 3000 rpm), 181 nm (5 wt%, 3000 rpm) and 305 nm (5 wt%, 1000 rpm), respectively. After one day of dying, the spin-coated films were annealed at an elevated temperature (1 h) in the range of 230–270 °C. The heating rate from room temperature to the target temperature was 10–12 °C min^{-1}.

Films of various thicknesses were deposited on bare SiO_x/Si substrates. The bare SiO_x/Si substrates have a hydrophilic surface enriched with hydroxyl groups. Prior to polymer deposition, the SiO_x/Si substrates were cleaned in piranha solutions (at 95 °C for 50 min), rinsed with deionized water and then exposed to UV-ozone (5 min).

For the annealed films, self-assembled nanodomains tend to adopt parallel orientation on SiO_x/Si. Thus, there should be a PS overlayer on the surface. To remove the surface wetting layer, oxygen plasma etching was imposed on the thin films on SiO_x/Si for 60–150 s at 10 sccm of oxygen flow rate and 90 W of power.

2.2. Material characterization

Surface morphologies of thin films of neat PS-*b*-PMMA and its blends with PS were characterized using an optical microscope

 This journal is © The Royal Society of Chemistry 2021

Published on 09 September 2021. Downloaded by National Synchrotron Radiation Research on 11/8/2021 6:47:33 AM.

(OM, Olympus BX-BLA2) in the reflection mode and an atomic force microscope (AFM, SPA400 Seiko) in the tapping mode. Side-view morphologies were characterized by field-emission scanning electron microscopy (FE-SEM, Hitachi SU8200), which was performed at 10 keV. Structural details in reciprocal space were characterized by grazing-incidence small-angle X-ray scattering (GISAXS) at TLS 23A of the National Synchrotron Radiation Research Center (NSRRC), Hsinchu. An incident angle (α_i) of 0.17° was used when an energy (E) of 10 keV of synchrotron-based X-rays was used for GISAXS measurements at TLS 23A. Reciprocal-space scattering and diffraction signals were collected using a Pilatus 2D area detector. The output data are GISAXS 2D images with intensity as the functions of $q_{\parallel}$ and $q_{\perp}$, where $q_{\parallel}$ and $q_{\perp}$ denote the scattering momentum vector along the lateral and normal directions, respectively. A standard sample, silver behenate, was used for the calibration of the sample-to-detector distance and scattering momentum vector.

3. Results and discussion

3.1. Self-assembly of the P(S-*b*-MMA)/PS blend films on SiO_x/Si

We first prepared thin films of the neat P(S-*b*-MMA) and its blends with PS of various weight fractions. The initial thickness (h_i) was 97 nm for the thin films, all of which were spin coated on SiO_x/Si. The ϕ_{PS} values are 52% [*i.e.* neat P(S-*b*-MMA)], 55%, 64% and 77%, respectively, for the P(S-*b*-MMA)/PS blends. The SiO_x/Si substrates have an attractive surface to the PMMA block. To develop self-assembled nanodomains, the thin films were annealed at 230 °C for 1 h. The thin films were then characterized by OM and AFM for surface morphological observations. Fig. S1 (ESI†) shows the OM images of the resultant films. As Fig. S1 (ESI†) shows, some of the prepared thin films form surface relief micro-terraces (*i.e.*, holes and islands). This result indicates that the films form parallel nanodomains on SiO_x/Si. Furthermore, because SiO_x/Si is a selective substrate, there must be a wetting layer with the PMMA chains anchoring the substrate interface through a polar interaction. Thus, the formation of relief micro-terraces is due to the incommensurability effect between the inter-domain spacing and initial film thickness. If the initial thickness of a film is incommensurate with the inter-domain spacing, thermal annealing inevitably causes film undulation to form surface micro-terraces with height or depth being commensurate with the integers of inter-domain spacing. The film incommensurability reported here differs from dewetting, which frequently leads to round islands or irregular holes with rims in a film when the film has a negative spreading coefficient on a solid substrate. In our study, the surface relief micro-terraces display step-like shapes rather than round shapes. For example, Fig. S2 (ESI†) shows the morphology of a terraced island in a film of the neat lamellae-forming P(S-*b*-MMA). On average, each step has a height of $\sim 26.6 \pm 0.2$ nm. The height matches the inter-layer distance of lamellae. Furthermore, no rims are present on the edge of the surface relief micro-terraces. Therefore, dewetting is excluded for the formation of surface relief micro-terraces.

Fig. S3 (ESI†) shows the representative AFM images of the thin films on SiO_x/Si before and after oxygen plasma etching. As the left panel of Fig. S3 (ESI†) shows, without oxygen plasma etching, the free surface of the thin films on SiO_x/Si is inevitably dominated by a PS overlayer. Thus, their pristine surface reveals a featureless morphology (see the left panel of Fig. S3, ESI†). To explore the inner nanodomains underneath the free surface by AFM, a subsequent etch through the PS overlayer is necessary. Except for the neat symmetric P(S-*b*-MMA) film, oxygen plasma etching was imposed on the blend films of P(S-*b*-MMA)/PS. As Fig. 1c, d and Fig. S3B and C (ESI†) show, the inner structures emerge after the removal of the overlayer. Two different morphologies are observed for the blend films with ϕ_{PS} = 64% and 77%, respectively. The first morphology is dot-like nanodomains with hexagonal arrays observed for the blend

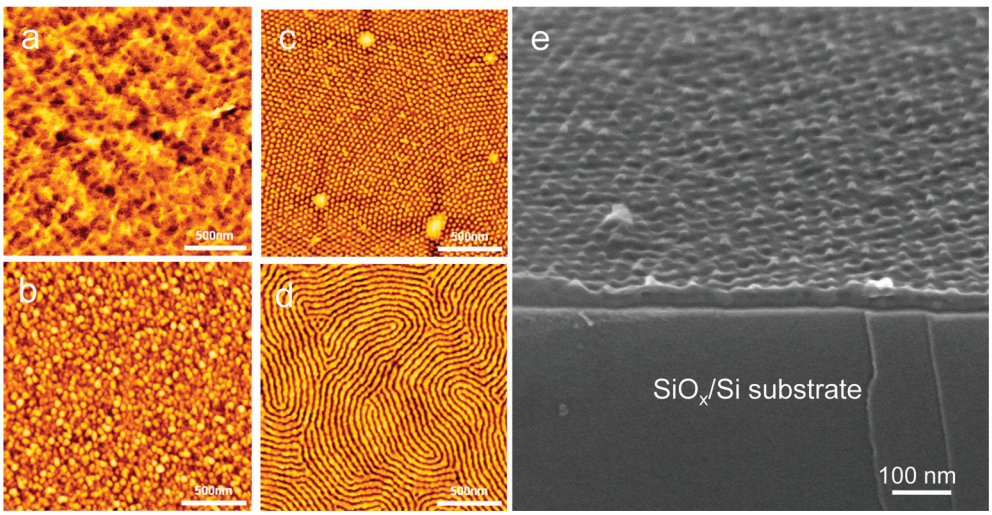

Fig. 1 AFM topographic images of thin films (h_i = 97 nm on SiO_x/Si) of P(S-*b*-MMA)/PS blends with various ϕ_{PS}: (a) 52%, (b) 55%, (c) 64% and (d) 77%. (e) 25°-Titled FE-SEM images of a thin film of P(S-*b*-MMA)/PS with ϕ_{PS} = 64%. Images b–e were collected with AFM or FE-SEM after oxygen plasma etching.

Published on 09 September 2021. Downloaded by National Synchrotron Radiation Research on 11/8/2021 6:47:33 AM.

film ϕ_{PS} = 64% (Fig. 1c and Fig. S3B, ESI†). The dot-like nanodomains appear convex and are analogous to short standing pillars (Fig. 1e). The second morphology is fingerprint-like nanodomains observed for the blend film ϕ_{PS} = 77% (Fig. 1d and Fig. S3C, ESI†).

In contrast, oxygen plasma etching only roughens the free surface for the blend film with ϕ_{PS} = 55% on SiO_x/Si (Fig. 1b and Fig. S3A, ESI†). Thus, both the surface roughness and the spatial correlation length increase with the increasing etching time (Fig. S4 and S5, ESI†). A quantitative analysis of the height profiles demonstrates that the root-mean-square (RMS) roughness was increased from 0.22 nm (before etching) to 1.56 nm (after etching of 60 s). Like the neat P(S-*b*-MMA) film, the thin blend film with ϕ_{PS} = 55% still forms parallel lamellae, thus displaying surface roughening after oxygen plasma etching (Fig. 1b and Fig. S3A, ESI†).

The thin blend film ϕ_{PS} = 64% tends to form perforated layers, in which the PS component not only formed layers but also formed perforations embedded with the PMMA layers (Fig. 1c and Fig. S3B, ESI†). Parallel orientation was also favored for the perforated layers on SiO_x/Si. Thus, the free surface was preferentially wetted by a PS overlayer followed by a periodic series of alternating layers of PMMA and PS. As a result, within every PMMA layer, PS perforations existed with extensions from two neighboring parallel PS layers. Furthermore, PS perforations in the parallel perforated layers had in-plane spatial order of hexagonal arrays. As reported in the literature, PMMA removal is considerably quicker than PS removal during oxygen plasma etching.[64] If the blend film with ϕ_{PS} = 64% formed perpendicular PMMA cylinders on SiO_x/Si, we should have observed dimple-like holes rather than convex nano-pillars. Therefore, we deduce that the relief dot-like nanodomains displayed in Fig. 1c correspond to PS perforations.

The blend film with ϕ_{PS} = 77% formed parallel cylinders. Oxygen plasma etching of the parallel cylinders produced fingerprint-like nanodomains (Fig. 1d and Fig. S3C, ESI†). The fingerprint-like nanodomains are more continuous and connective than their neighboring regions that display dark color and narrow width. Such a stark contrast is in line with previous observations reported by Campbell *et al.*[65,66] In our study, the color contrast indicates that those fingerprint-like nanodomains are composed of the PS matrix while the narrow regions with low height result from the quick removal of the PMMA nanodomains.

3.2. Spatial order of nanodomains on SiO_x/Si

Considering that AFM characterization only offers structural information over small areas and is limited to the surface of a film, we further carried out GISAXS measurements to characterize structural details over large areas for the thin films on SiO_x/Si. Fig. 2 shows the representative GISAXS 2D patterns of the prepared films on SiO_x/Si. Several prominent scattering features are present in the 2D patterns. The first prominent feature is a strong diffuse scattering (indicated by an arrowhead) near the shadow of the beam stopper in particular for the etched P(S-*b*-MMA)/PS blend films (Fig. 2b). This strong diffuse scattering should result from the roughened surface as the result of oxygen plasma etching. Besides, a series of parallel streaks of scattering (highlighted by dotted boxes in Fig. 2b-d) associated with standing waves are present along the $q_\perp$ direction. The series of parallel scattering streaks has been ascribed to the interplay between the refractive and reflective effects at both surfaces and interfaces.[67]

The third feature is the presence of diffraction truncation rods along the $q_\parallel$ direction. Those diffraction truncation rods appear with extended scattering intensity perpendicular to the surface, a typical feature of topographic surface structures resulted from oxygen plasma etching. However, this feature was not expected for the P(S-*b*-MMA)/PS (ϕ_{PS} = 52% and 55%) films (Fig. 2a and b). The unexpected feature implies that some local areas of the two films must have formed perpendicular lamellae on SiO_x/Si. The perpendicular lamellae formed on SiO_x/Si might be due to the confinement effect. Previous studies have demonstrated that if the initial thickness of the film is incommensurate with the domain spacing, perpendicular lamellae may form and coexist with parallel lamellae even on a selective substrate.[11,12] Another possible reason is that with no or a small amount of the low-molecular-weight PS, the free surface of the two lamellae-forming films may reach a neutral condition when annealed at 230 °C. This behavior is

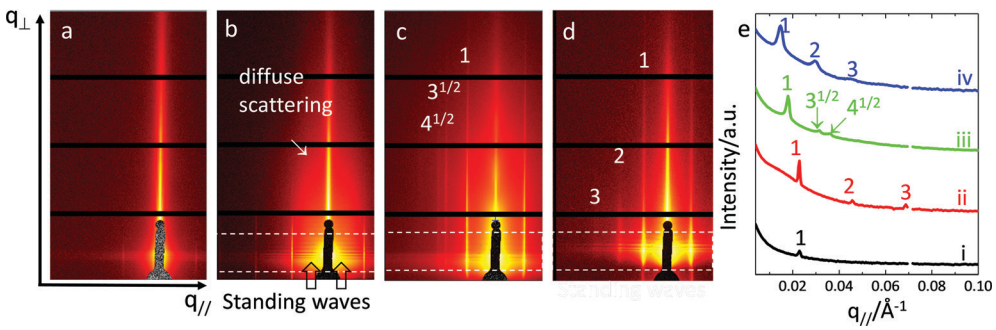

Fig. 2 (a–d) GISAXS 2D patterns (collected at α_i = 0.17° and E = 10 keV) and (e) 1D corresponding profiles of thin films (h_i = 97 nm on SiO_x/Si) of P(S-*b*-MMA)/PS blends of various ϕ_{PS}s: 52% (a, e-i), 55% (b and e-ii), 64% (c and e-iii) and 77% (d and e-iv), respectively. All the thin blend films were annealed at 230 °C (1 hour). Note that samples b–d were exposed to oxygen plasma etching for 60 s. Positions of the truncated Bragg rods/peaks are labelled according to their $q_\parallel$ positions, and standing waves are highlighted by dotted boxes for a visual guide.

 This journal is © The Royal Society of Chemistry 2021

Published on 09 September 2021. Downloaded by National Synchrotron Radiation Research on 11/8/2021 6:47:33 AM.

related to the observations by the Russell group studying the absence of surface segregation for other P(S-*b*-MMA) BCPs annealed above 225 °C.[68] Thus, the formation of perpendicular lamellae observed for the neat and blend films with ϕ_{PS} = 55% on SiO_x/Si is ascribed to the interplay between the neutral surface, selective interface and confinement. Nevertheless, the perpendicular lamellae should only exist in minor while the parallel lamellae should exist in major for the two lamellae-forming films on SiO_x/Si. Therefore, the AFM characterization more frequently detected parallel lamellae but rarely detected perpendicular lamellae.

Quantitatively analyzing the GISAXS data of the thin blend film of ϕ_{PS} = 64% demonstrates that the diffraction truncation rods have a positional ratio $\left(q_{\parallel}/q_{\parallel}^{*}\right)$ of $1:3^{1/2}:4^{1/2}$, where $q_{\parallel}^{*}$ is the first-order rod centered at 0.0179 $Å^{-1}$ (Fig. 2c and 2e-iii). This positional ratio indicates that the PS perforations in parallel perforated layers on SiO_x/Si have long-range order of hexagonal arrays.

For the thin blend film with ϕ_{PS} = 77%, its GISAXS 2D pattern and the corresponding 1D profile display diffraction truncation rods and peaks in series with a positional ratio of $1:2:3$, where the $3^{1/2}$ peak is absent and the first-order peak is at $q_{\parallel}^{*}$= 0.0146 $Å^{-1}$ (Fig. 2d and e-iv). The absence of the $3^{1/2}$ peak indicates that the parallel cylinders confined within the thin blend film with ϕ_{PS} = 77% on SiO_x/Si lack out-of-plane spatial order of hexagonal arrays. Note that no intensity modulation is present along the $q_{\perp}$ direction for the truncation rods of the parallel perforated layers and cylinders. The scattering stems from the volume of the thin films because the incident angle is higher than the critical angle of the polymers.

Fig. 3 summarizes the phase behavior of a series of P(S-*b*-MMA)/PS thin films (h_i = 97 nm) with PS compositions, 52% < ϕ_{PS} < 77%, on SiO_x/Si. As Fig. 3 shows, lamellae formed in thin films with 52% < ϕ_{PS} < 62% and parallel cylinders formed in thin films with 67% < ϕ_{PS} < 77% if thermal annealing is performed at 230 °C for 1 h. As compared to the lamella and cylinder phases, the perforated layer phase only exists at a narrow window (64% < ϕ_{PS} < 67%) under the same course of thermal annealing; however, at ϕ_{PS} = 67%, both the perforated layers and cylinders coexist in thin films.

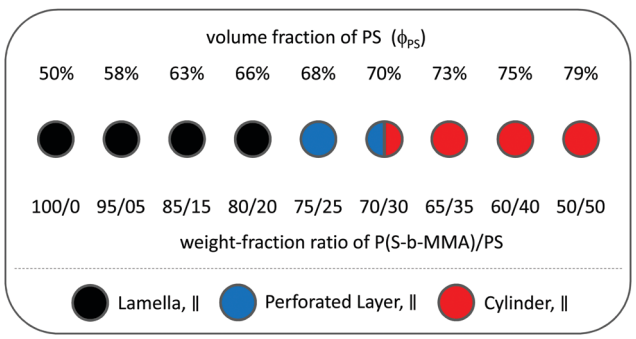

Fig. 3 Phase behavior of P(S-*b*-MMA)/PS thin films (h_i = 97 nm on SiO_x/Si) as a function of ϕ_{PS}. All the films were annealed at 230 °C for 1 hour.

3.3. Effects of thickness and temperature on the formation of perforated layers

For hexagonally perforated layers (HPL), hexagonal arrays with either AB or ABC stacking have been frequently reported by experimental results[27–30] or theoretical calculations.[32–34] A previous study has demonstrated that for neat BCPs, HPL is a long-life metastable phase in bulk whereas a double gyroid with low packing frustration is a stable phase in bulk.[34] The metastability of HPL is due to high packing frustration. However, homopolymer addition,[43,44] spatial confinement and surface fields[2–8] have been found to steadily stabilize HPL. Therefore, a combination of the three additional factors should make the phase behavior of copolymer/homopolymer mixtures in thin films more complicated and diverse. To the best of our knowledge, only little effort has been made to study the phase behavior of perforated layers *versus* double gyroid in thin films of copolymer/homopolymer binary blends as compared to the classic lamella, cylinder and sphere phases. To investigate the effects of temperature and thickness on the stability of perforated layers, we prepared another series of P(S-*b*-MMA)/PS blend films, for which three initial thicknesses (97, 181 and 305 nm) were prepared and the PS composition in blends was fixed at ϕ_{PS} = 64%. The thicknesses approximately correspond to n = 3.3, 6.1 and 10.3, respectively, where n denotes the number of layers defined by the ratio of the initial thickness to the interlayer spacing of perpendicular perforated layers.[69] The P(S-*b*-MMA)/PS blend films with ϕ_{PS} = 64% were then annealed at a temperature in the range of 230–270 °C for 1 h each. The temperature range corresponds to a range of segregation strength from χN = 15.25 at 230 °C to χN = 14.98 at 270 °C. This range of χN was estimated according to the expression of temperature-dependent χ given by,[70]

$$\chi = 0.0282 + \frac{4.46}{T} \quad (1)$$

and the molecular weight of the constituent blcoks. This χN range thus corresponds to the weak segregation region for films annealed at 230–270 °C (*i.e.*, T = 503–543 K)

After annealing at 230 °C for 1 hour, the blend films with ϕ_{PS} = 64% were further treated by oxygen plasma etching (60–150 s) for morphological observations with AFM and for structural characterization with GISAXS. Fig. 4 shows the representative AFM images and GISAXS patterns obtained from three 230 °C-annealed films, whose initial thickness was 97, 181 and 305 nm, respectively. Regardless of the different thicknesses, the films annealed at 230 °C tended to form perforated layers. Upon overlayer removal, the PS perforations can be easily identified with AFM (Fig. 4a–c). The PS perforations confined within parallel layers have spatial order of hexagonal arrays. Because of surface topography, the PS perforations exhibit three Bragg truncation rods, which exhibit extended intensity along the $q_{\perp}$ direction in Fig. 4d–f. The positions of the rods are indexed with $1:3^{1/2}:4^{1/2}$ on the basis of hexagonal arrays (Fig. 4d–g).

In contrast, annealing at 270 °C produced different morphologies in P(S-*b*-MMA)/PS blend films with ϕ_{PS} = 64%.

Published on 09 September 2021. Downloaded by National Synchrotron Radiation Research on 11/8/2021 6:47:33 AM.

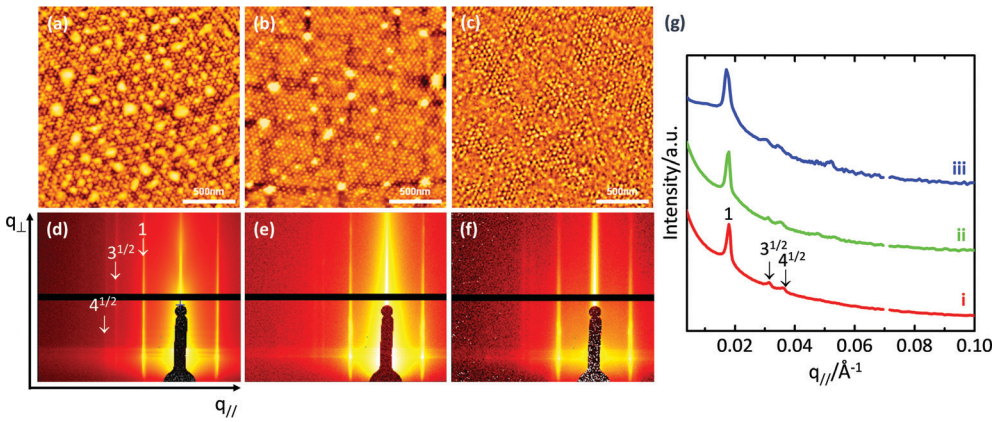

Fig. 4 (a–c) Representative AFM images and (d–g) GISAXS 2D/1D patterns (collected at α_i = 0.17° and E = 10 keV) for blend films of (a, d and g_i) h_i = 97 nm, (b, e and g_{ii}) 181 nm and (c, f and g_{iii}) 305 nm at ϕ_{PS} = 64%. The blend films were annealed at 230 °C for 1 hour and then treated by oxygen plasma etching for 60–150 s. Note that in some cases, oxygen plasma etching to remove the PS overlayer produces debris, displayed as tiny humps on the surface.

Fig. 5 shows the representative AFM images and GISAXS patterns of another set of films. The magnified version of Fig. 5b and c is also shown along with the corresponding phase images as Fig. S6 (ESI†) in the ESI for clarification. Three thicknesses, 97, 181 and 305 nm, were prepared for thermal annealing at 270 °C. Interestingly, films of h_i = 97 nm only formed hexagonally perforated layers (Fig. 5a). However, a mixture of double gyroid and perforated layers was obtained for films of h_i = 181 nm (Fig. 5b). Upon annealing at 270 °C, films of h_i = 305 nm only formed double gyroid (Fig. 5c). The PS matrix of the double gyroid displays a double-wave pattern (Fig. 5c). The porous channels resulted from PMMA removal display a zigzag-like pattern in the phase image (Fig. S6, ESI†). Both the double-wave and zigzag-like patterns indicate that the $\{121\}_{DG}$ lattice planes are oriented parallel to SiO_x/Si.

To demonstrate the spatial order of the observed nanodomains over a large area, we further performed GISAXS characterization. As Fig. 5d and gi show, the perforated layers show a series of diffraction truncation rods with a $q_{\|}/q_{\|}^*$ ratio of $1:3^{1/2}:4^{1/2}$, where $q_{\|}^*$ denotes the position of the first peak. This ratio is ascribed to the hexagonal packing of PS perforations. For the films of h_i = 181 and 305 nm, the GISAXS patterns are mainly contributed by double gyroids with the $\{121\}_{DG}$ lattice planes being parallel to the substrate (Fig. 5e and f). Thus, several diffraction truncation rods associated with double gyroids are present in Fig. 5e and f. Due to oxygen plasma etching, all the reflections display intense intensity that extends toward high $q_\perp$. Hence, the intensity extending can be ascribed to the surface relief topography of a thinned thickness. The thinned thickness is due to the anisotropic etching under oxygen plasma treatment. In other words, the etching rate is higher along the normal direction than along the in-plane direction of the substrate. Because the extent of intensity extending is inversely proportional to the thickness, the nanostructures of a thinned thickness scatter truncation rods with a high extent of intensity extending. In addition to the intense truncation rods that resulted from the extension of the $\{121\}_{DG}$

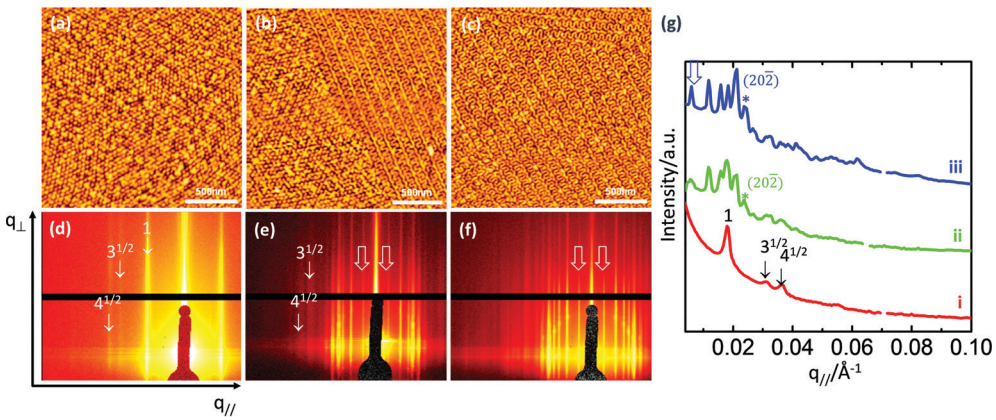

Fig. 5 (a–c) Representative AFM images and (d–g) GISAXS 2D/1D patterns (collected at α_i = 0.17° and E = 10 keV) for blend films of (a, d and g_i) h_i = 97, (b, e and g_{ii}) 181 and (c, f and g_{iii}) 305 nm at ϕ_{PS} = 64%. The films were annealed at 270 °C for 1 hour and then treated by oxygen plasma etching for ≥60 s. The asterisks (*) on curves g_{ii} and g_{iii} indicate the position of the $(20\bar{2})$ peak.

 This journal is © The Royal Society of Chemistry 2021

Published on 09 September 2021. Downloaded by National Synchrotron Radiation Research on 11/8/2021 6:47:33 AM.

and {220} diffraction spots at low $q_{\parallel}$, two diffraction truncation rods associated with the hexagonal arrays of relief perforations appear at high $q_{\parallel}$. Thus, such a GISAXS pattern confirmed that both the double gyroid and perforated layers were obtained for the 270 °C-annealed film of h_i = 181 nm. Furthermore, the content of perforated layers should be comparable to the content of double gyroids. In comparison, for the thick film of h_i = 305 nm, the diffraction rods/spots associated with the double-gyroid phase are more intense than those associated with the perforated-layer phase. This result indicates that as the thickness increases, the double gyroid becomes a dominant phase. Note that an additional truncation rod appears at a very low $q_{\parallel}$ (indicated by thick arrowheads). The truncations should be the {110} reflections, which are ascribed to the anisotropic deformation of the films.[71] The anisotropic deformation may further cause the distortion of cubic cells in the double-gyroid phase. In fact, the distortion of double-gyroid unit cells has been frequently found to exist in thin films.[71,72] As a rough estimate, the lattice parameter of the cubic unit cell was calculated as a_{DG} = 73.5 nm on the basis of $a_{DG} = \left(2\pi \times 2\sqrt{2}\right) \Big/ q_{\parallel,(20\bar{2})}$,[73] where the $(20\bar{2})$ peak is centered at $q_{\parallel,(20\bar{2})} \sim 0.02419$ Å^{-1}.

According to the AFM and GISAXS characterization of the blend films, we summarize the morphologies in Fig. 6. The figure shows the obtained morphologies as a function of film thickness and temperature in blend films of P(S-*b*-MMA)/PS at ϕ_{PS} = 64%. In Fig. 6, we classified three regions (regions-I, -II and -III) according to the morphologies. Region-I includes the films of h_i = 97 nm that were annealed at 230–270 °C and films of h_i = 181 and 305 nm that were annealed at 230 °C (Fig. 6). Perforated layers solely existed as a single phase in region-I.

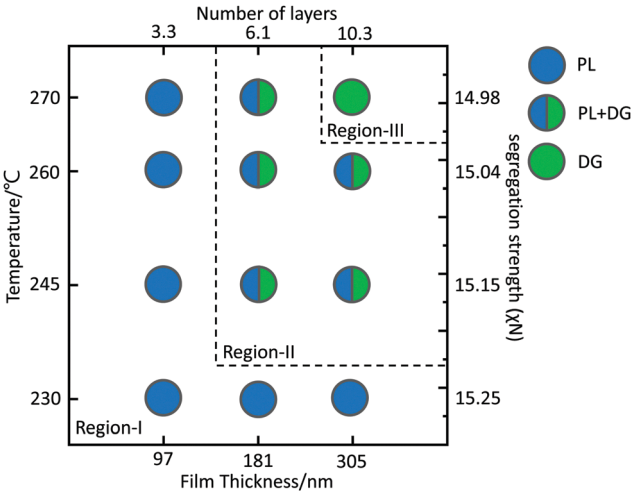

Fig. 6 Phase behavior of films of a P(S-*b*-MMA)/PS binary blend with ϕ_{PS} = 64% as a function of annealing temperature/segregation strength (left and right axes) and film thickness/layer number (top and bottom axes). The perforated-layer phase is represented by blue symbols and the double-gyroid phase is represented by green symbols. Note that the dotted lines are used only for the visual guidance of regions-I/-II/-III and do not reflect phase boundaries.

The forbidden DG phase in the films of h_i = 97 nm is due to the confinement effect. On the basis of the $(20\bar{2})$ peak, the structural parameter of the cubic lattice was approximately estimated as $a_{DG} \sim 73.5$ nm. If it is further considered that there must be an anchoring layer near the substrate interface, it is expected that steadily forming the DG phase with $a_{DG} \sim 73.5$ nm needs a higher thickness. The anchoring layer is possible because the SiO_x/Si substrate has a strong affinity to the PMMA block. Our previous studies demonstrated that the anchoring layer is a layer-like structure, and that its morphology also deviates from the morphology of self-assembled nanodomains on top of the anchoring layer.[74,75] The possibility of an anchoring layer forming near the substrate interface explains why the DG phase is totally absent even at h_i = 97 nm. Although the DG phase may deform to adapt to the confined space by forming a triclinic DG phase, lattice deformation inevitably leads to a high entropic penalty. If there is a mismatch between the initial film thickness and the integers of a_{DG}, the DG phase cannot form. Furthermore, the DG phase is an ordered there-dimensional network structure comprising triple connectors whereas parallel perforated layers are analogous to the two-dimensional structure of alternating layers. It is likely that perforated layers are favored under one-dimensional spatial confinement.

In contrast, region-II is a two-phase region where double gyroid and perforated layers are concurrently formed. Region-II includes films of h_i= 181 nm that were annealed at 245–260 °C and films of 305 nm that were annealed at 245–270 °C. Although the perforated layers and double gyroids coexisted in region-II, their contents were found to vary at different temperatures. As a result, annealing at 270 °C tended to favor a high content of double gyroids while annealing at 245 °C tended to favor a high content of perforated layers. The stability of the PL phase strongly depends on the film thickness and thermal-annealing temperature. Upon increasing the thickness and temperature, DG nanodomains with $\{121\}_{DG}$ parallel to the substrate surface become dominant over HPL. The double gyroid became the only discernible phase if films of h_i = 305 nm were annealed at 270 °C (region-III).

We also tested if the perforated-layer and double gyroid phases could form in films that were prepared by blending high-molecular-weight symmetric P(S-*b*-MMA) BCPs with the low-molecular-weight PS at ϕ_{PS} = 64% followed by annealing at 230 or 270 °C. As Fig. S7 and S8 (ESI†) show, neither perforated layers nor double gyroids were obtained for the films at ϕ_{PS} = 64%. Instead, only cylinders of mixed orientations formed on SiO_x/Si. The mixed orientation is due to the competitive interplay between the neutral free surface and the selective substrate interface.

The absence of the PL and DG phases from the films containing the high-molecular-weight P(S-*b*-MMA) BCPs can be ascribed to the increase in χN. The increased χN arises from the high-molecular-weight PS-*b*-PMMA BCPs in the P(S-*b*-MMA)/PS mixtures. It has been proposed that high χN magnifies the packing frustration.[34] Under high χN, the stretching of polymer chains becomes too difficult to fill the corners of the

Published on 09 September 2021. Downloaded by National Synchrotron Radiation Research on 11/8/2021 6:47:33 AM.

Wigner–Seitz cell. As a result, such high packing frustration cannot be alleviated by the addition of homopolymer chains. Our result is parallel to previous findings[34] that increasing χN amplifies the packing frustration. Since cylinders have a lower packing frustration than perforated layers, the cylinder phase is dominant over the perforated-layer phase in thin blend films that were prepared from binary blends of high-molecular-weight P(S-*b*-MMA) BCPs with PS (Fig. S7 and S8, ESI†) under ϕ_{PS}= 64%.

4. Conclusions

We have demonstrated that a series of morphologies were obtained for thin films of P(S-*b*-MMA)/PS mixtures with various ϕ_{PS} on SiO_x/Si. Parallel lamellae dominate at $52\% < \phi_{PS} < 62\%$ whereas parallel cylinders dominate at $67\% < \phi_{PS} < 77\%$. In comparison, parallel perforated layers only exist at a narrow region, ϕ_{PS} = 64%. Furthermore, at ϕ_{PS} = 64%, tuning film thickness and annealing temperature can produce parallel perforated layers and/or double gyroid with $\{121\}_{DG}$ lattice planes being parallel to the substrate surface. The effects of annealing temperature and film thickness on the (meta)stability of perforated layers and double gyroid were examined. In thin films with n = 3.3, perforated layers solely existed as a stable phase regardless of annealing temperature. However, for thick films with n = 6.1 and 10.3, thermal annealing at the most accessible temperature produces films containing both perforated layers and double gyroid phases of various fractions, but a low temperature tends to favor greater fractions of perforated layers. The perforated layers become the only discernible phase if thick films are annealed at 230 °C.

Author contributions

Conceptualization: Y. S. Sun; data curation: J. W. Hong and J. H. Chang; formal analysis: J. W. Hong; funding acquisition: Y. S. Sun; investigation: J. W. Hong and I. C.-Y. Chang; supervision: Y. S. Sun; visualization: J. W. Chang; writing-original draft: Y. S. Sun; writing-review & editing: Y. S. Sun.

Conflicts of interest

All the authors have no conflicts of interest.

Acknowledgements

Financial support from the Ministry of Science and Technology (MOST 107-2221-E-008-034-MY3) is gratefully acknowledged. We also thank Dr Chun-Jen Su and Dr U-Ser Jeng for their kind assistance in the GISAXS experiments at TLS BL23A of NSRRC.

References

1 M. W. Matsen and F. S. Bates, *Macromolecules*, 1996, **29**, 1091–1098.
2 A. Knoll, A. Horvat, K. S. Lyakhova, G. Krausch, G. J. A. Sevink, A. V. Zvelindovsky and R. Magerle, *Phys. Rev. Lett.*, 2002, **89**, 035501.
3 H. P. Huinink, J. C. M. Brokken-Zijp and M. A. van Dijk, *J. Chem. Phys.*, 2000, **112**, 2452–2462.
4 A. Knoll and R. Magerle, *J. Chem. Phys.*, 2004, **120**, 1105–1116.
5 A. Horvat, K. S. Lyakhova, G. J. A. Sevink, A. V. Zvelindovsky and R. Magerle, *J. Chem. Phys.*, 2004, **120**, 1117–1126.
6 A. Knoll, K. S. Lyakhova, A. Horvat, G. Krausch, G. J. A. Sevink, A. V. Zvelindovsky and R. Magerle, *Nat. Mater.*, 2004, **3**, 886–890.
7 K. S. Laykhova, G. J. A. Sevink, A. V. Zvenlindovsky, A. Horvat and R. Magerle, *J. Chem. Phys.*, 2004, **120**, 1127–1137.
8 H. P. Huinink, M. A. Van Dijk, J. C. M. Brokken-Zijp and G. J. A. Sevink, *Macromolecules*, 2001, **34**, 5325–5330.
9 M. J. Fasolka and A. M. Mayes, *Annu. Rev. Mater. Res.*, 2001, **31**, 323–355.
10 M. W. Matsen, *J. Chem. Phys.*, 1997, **106**, 7781–7791.
11 M. J. Fasolka, P. Banerjee, A. M. Mayes, G. Pickett and A. Balazs, *Macromolecules*, 2000, **33**, 5702–5712.
12 T. L. Morkved and H. M. Jaeger, *Europhys. Lett.*, 1997, **40**, 643–648.
13 K. Sparnacci, D. Antonioli, V. Gianotti, M. Laus, F. F. Lupi, T. J. Giammaria, G. Seguini and M. Perego, *ACS Appl. Mater. Interfaces*, 2015, **7**, 10944–10951.
14 F. F. Lupi, T. J. Giammaria, G. Seguini, F. Vita, O. Francescangeli, K. Sparnacci, D. Antonioli, V. Gianotti, M. Laus and M. Perego, *ACS Appl. Mater. Interfaces*, 2014, **6**, 7180–7188.
15 S. Ham, C. Shin, E. Kim, D. Y. Ryu, U. Jeong and T. P. Russell, C. J. Hawker, *Macromolecules*, 2008, **41**, 6431–6437.
16 E. Huang, T. P. Russell, C. Harrison, P. M. Chaikin, R. A. Register, C. J. Hawker and J. Mays, *Macromolecules*, 1998, **31**, 7641–7650.
17 E. Huang, S. Pruzinsky, T. P. Russell, J. Mays and C. J. Hawker, *Macromolecules*, 1999, **32**, 5299–5303.
18 R. Guo, E. Kim, J. Gong, S. Choi, S. Ham and D. Y. Ryu, *Soft Matter*, 2011, **7**, 6920–6925.
19 S. Ji, W. Liao and P. F. Nealey, *Macromolecules*, 2010, **43**, 6919–6922.
20 E. Han, K. O. Stuen, M. Leolukman, C. C. Liu, P. F. Nealey and P. Gopalan, *Macromolecules*, 2009, **42**, 4896–4901.
21 M. S. She, T. Y. Lo and R. M. Ho, *ACS Nano*, 2013, **7**, 2000–2011.
22 G. E. Stein, E. J. Kramer, X. Li and J. Wang, *Macromolecules*, 2007, **40**, 2453–2460.
23 V. Mishra, S. M. Hur, E. W. Cochran, G. E. Stein, G. H. Fredrickson and E. J. Kramer, *Macromolecules*, 2010, **43**, 1942–1949.
24 G. E. Stein, E. W. Cochran, K. Katsov, G. H. Fredrickson, E. J. Kramer, X. Li and J. Wang, *Phys. Rev. Lett.*, 2007, **98**, 158302.
25 J. Jung, H. W. Park, S. Lee, H. Lee, T. Chang, K. Matsunaga and H. Jinnai, *ACS Nano*, 2010, **4**, 3109–3116.
26 C. H. Hsu, K. Yue, J. Wang, X. H. Dong, Y. F. Xia, Z. Jiang, E. L. Thomas and S. Z. D. Cheng, *Macromolecules*, 2017, **50**, 7282–7290.

 This journal is © The Royal Society of Chemistry 2021

Published on 09 September 2021. Downloaded by National Synchrotron Radiation Research on 11/8/2021 6:47:33 AM.

27 I. W. Hamley, K. A. Koppi, J. H. Rosedale, F. S. Bates, K. Almdal and K. Mortensen, *Macromolecules*, 1993, **26**, 5959–5970.
28 S. Föerster, A. K. Khandpur, J. Zhao, F. S. Bates, I. W. Hamley, A. J. Ryan and W. Bras, *Macromolecules*, 1994, **27**, 6922–6935.
29 A. K. Khandpur, S. Foerster, F. S. Bates, I. W. Hamley, A. J. Ryan, W. Bras, K. Almdal and K. Mortensen, *Macromolecules*, 1995, **28**, 8796–8806.
30 D. A. Hajduk, H. Takenouchi, M. A. Hillmyer, F. S. Bates, M. E. Vigild and K. Almdal, *Macromolecules*, 1997, **30**, 3788–3795.
31 N. Ji, P. Tang, F. Qiu and A.-C. Shi, *Macromolecules*, 2015, **48**, 8681–8693.
32 M. Laradji, A. C. Shi, J. Noolandi and R. C. Desai, *Macromolecules*, 1997, **30**, 3242–3255.
33 S. Qi and Z. G. Wang, *Macromolecules*, 1997, **30**, 4491–4497.
34 M. W. Matsen and F. S. Bates, *Macromolecules*, 1996, **29**, 7641–7644.
35 Y. Kim, D. Yong, W. Lee, S. Jo, H. Ahn, J. U. Kim and D. Y. Ryu, *Macromolecules*, 2018, **51**, 8550–8560.
36 C. Shin, H. Ahn, E. Kim, D. Y. Ryu, J. Huh, K. W. Kim and T. P. Russell, *Macromolecules*, 2008, **41**, 9140–9145.
37 V. Mishra, G. H. Fredrickson and E. J. Kramer, *ACS Nano*, 2012, **6**, 2629–2641.
38 S. Choi, E. Kim, H. Ahn, S. Naidu, Y. Lee, D. Y. Ryu, C. J. Hawker and T. P. Russell, *Soft Matter*, 2012, **8**, 3463–3469.
39 S. W. Kim, E. Kim, H. Lee, B. C. Berry, H. C. Kim and D. Y. Ryu, *Polymer*, 2015, **74**, 63–69.
40 T. Hashimoto, H. Tanaka and H. Hasegawa, *Macromolecules*, 1990, **23**, 4378–4386.
41 H. Tanaka, H. Hasegawa and T. Hashimoto, *Macromolecules*, 1991, **24**, 240–251.
42 K. I. Winey, E. L. Thomas and L. J. Fetters, *J. Chem. Phys.*, 1991, **95**, 9367–9375.
43 M. W. Matsen, *Macromolecules*, 1995, **28**, 5765–5773.
44 M. W. Matsen, *Phys. Rev. Lett.*, 1995, **74**, 4225–4228.
45 Y. Y. Huang, H. L. Chen and T. Hashimoto, *Macromolecules*, 2003, **36**, 764–770.
46 C. Y. Chu, R. Y. Pei and H. L. Chen, *Macromolecules*, 2018, **51**, 8493–8500.
47 H. F. Wang, L. H. Yu, X. B. Wang and R. M. Ho, *Macromolecules*, 2014, **47**, 7993–8001.
48 S. Valkama, O. Lehtonen, K. Lappalainen, H. Kosonen, P. Castro, T. Repo, M. Torkkeli, R. Serimaa, G. ten Brinke, M. Leskelä and O. Ikkala, *Macromol. Rapid Commun.*, 2003, **24**, 556–560.
49 I. Vukovic, H. Friedrich, D. H. Merino, G. Portale, G. ten Brinke and K. Loos, *Macromol. Rapid Commun.*, 2013, **34**, 1208–1212.
50 U. Jeong, D. Y. Ryu, D. H. Kho, D. H. Lee, J. K. Kim and T. P. Russell, *Macromolecules*, 2003, **36**, 3626–3634.
51 U. Jeong, D. Y. Ryu, D. H. Kho, J. K. Kim, J. T. Goldbach, D. H. Kim and T. P. Russell, *Adv. Mater.*, 2004, **16**, 533–536.
52 M. P. Stoykovich, M. Müller, S. O. Kim, H. H. Solak, E. W. Edwards, J. J. de Pablo and P. F. Nealey, *Science*, 2005, **308**, 1442–1446.
53 U. Nagpal, H. Kang, G. S. W. Craig, P. F. Nealey and J. J. de Pablo, *ACS Nano*, 2011, **5**, 5673–5682.
54 G. Liu, C. S. Thomas, G. S. W. Craig and P. F. Nealey, *Adv. Funct. Mater.*, 2010, **20**, 1251–1257.
55 M. P. Stoykovich, H. Kang, K. C. Daoulas, G. Liu, C. C. Liu, J. J. de Pablo, M. Müller and P. F. Nealey, *ACS Nano*, 2007, **1**, 168–175.
56 K. O. Stuen, C. S. Thomas, G. Liu, N. Ferrier and P. F. Nealey, *Macromolecules*, 2009, **42**, 5139–5145.
57 K. A. Orso and P. F. Green, *Macromolecules*, 1999, **32**, 1087–1092.
58 G. S. Doerk and K. G. Yager, *ACS Nano*, 2017, **11**, 12326.
59 G. S. Doerk, R. Li, M. Fukuto, A. Rodriguez and K. G. Yager, *Macromolecules*, 2018, **51**(24), 10259–10270.
60 S. Y. Yang, J. A. Yang, E. S. Kim, G. Jeon, E. J. Oh, K. Y. Choi, S. K. Hahn and J. K. Kim, *ACS Nano*, 2010, **4**, 3817–3822.
61 P. Zavala-Rivera, K. Channon, V. Nguyen, E. Sivaniah, D. Kabra, R. H. Friend, S. K. Nataraj, S. A. Al-Muhtaseb, A. Hexemer, M. E. Calvo and H. Miguez, *Nat. Mater.*, 2012, **11**, 53–57.
62 S. Park, Y. Kim, H. Ahn, J. H. Kim, P. J. Yoo and D. Y. Ryu, *Sci. Rep.*, 2016, **6**, 36326.
63 S. Park, Y. Kim, W. Lee, S. M. Hur and D. Y. Ryu, *Macromolecules*, 2017, **50**, 5033–5041.
64 R. A. Farrell, N. Petkov, M. T. Shaw, V. Djara, J. D. Holmes and M. A. Morris, *Macromolecules*, 2010, **43**(20), 8651–8655.
65 I. P. Campbell, G. J. Lau, J. L. Feaver and M. P. Stoykovich, *Macromolecules*, 2012, **45**, 1587–1594.
66 I. P. Campbell, S. Hirokawa and M. P. Stoykovich, *Macromolecules*, 2013, **46**, 9599–9608.
67 J. Wang, M. J. Bedzyk and M. Caffrey, *Science*, 1992, **258**, 775–778.
68 P. Mansky, T. P. Russell, C. J. Hawker, J. Mays, D. C. Cook and S. K. Satija, *Phys. Rev. Lett.*, 1997, **79**, 237–240.
69 For the P(S-*b*-MMA)/PS mixture at ϕ_{PS}, perforated layers preferentially formed perpendicular orientation in thin films (h_i = 97 nm) on a SiOx/Si substrate capped by a layer of neutralized PS chains. GISAXS characterization indicates that the long spacing is 29.7 nm for the perpendicular perforated layers.
70 Z. Zhao, E. Sivaniah and T. Hashimoto, *Macromolecules*, 2008, **41**, 9948–9951.
71 G. E. Toombes, A. C. Finnefrock, M. W. Tate, R. Ulrich, U. Wiesner and S. M. Gruner, *Macromolecules*, 2007, **40**, 8974–8982.
72 X. Feng, C. J. Burke, M. Zhuo, H. Guo, K. Yang, A. Reddy, I. Prasad, R.-M. Ho, A. Avgeropoulos, G. M. Grason and E. L. Thomas, *Nature*, 2019, **575**, 175–179.
73 B. Lee, I. Park, J. Yoon, S. Park, J. Kim, K. W. Kim, T. Chang and M. Ree, *Macromolecules*, 2005, **38**, 4311–4323.
74 Y. S. Sun, S. W. Chien and J. Y. Liu, *Macromolecules*, 2010, **43**, 7520–7560.
75 C. Y. Chang, P. J. Wu and Y. S. Sun, *Soft Matter*, 2011, **7**, 9140–9147.